RESEARCH ARTICLE | MARCH 07 2024

On the influence of spanwise deformation on lift coefficient and trailing vortices properties at low Reynolds number

P. Solis ; M. Garrido-Martin ; E. Duran ; P. Gutierrez-Castillo ; C. del Pino

Physics of Fluids 36, 037122 (2024)
https://doi.org/10.1063/5.0195188

Physics of Fluids ARTICLE pubs.aip.org/aip/pof

On the influence of spanwise deformation on lift coefficient and trailing vortices properties at low Reynolds number

Cite as: Phys. Fluids **36**, 037122 (2024); doi: 10.1063/5.0195188
Submitted: 31 December 2023 · Accepted: 8 February 2024 ·
Published Online: 7 March 2024

P. Solis, M. Garrido-Martin, E. Duran,[a] P. Gutierrez-Castillo, and C. del Pino

AFFILIATIONS

Fluid Mechanics Group, University of Málaga, Dr Ortiz Ramos s/n, 29071 Málaga, Spain

[a]Author to whom correspondence should be addressed: eduran@uma.es

ABSTRACT

We conducted experiments using a single non-deformed and two spanwise deformed wing models for a constant chord-based Reynolds number, $Re = 20 \times 10^3$. We carried out all experiments to consider several angles of attack α lower than the stall value. The lift forces between non-deformed and spanwise deformed wings present differences depending on the angle of attack. A first finding of the experimental study is that, for smaller values of the angle of attack, e.g., $\alpha = 4°$, the non-deformed wing case has higher lift values than the highest spanwise deformed wing. However, for larger values of the angle of attack, such as $\alpha = 8°$, we found a higher lift for the spanwise deformed case. Additionally, velocity fields of the trailing vortex have been taken by two-dimensional particle image velocimetry, finding that both theoretical models by Batchelor [J. Fluid Mech. 20, 645 (1964)] and by Moore and Saffman [Proc. R. Soc. Lond. Ser. A 333, 491 (1973)] can be fitted to experimental measurements obtained from non-deformed and spanwise deformed wing models, the latter model giving the best results for all angles of attack. Finally, we computed the circulation of the trailing vortex using two different methods with the same result and observing that this estimated circulation level directly correlates with the measurement of the lift force.

I. INTRODUCTION

The state-of-the-art on steady aerodynamics under subsonic flow conditions has many examples of researchers performing force measurements on a stiff-wing configuration.[1,5,16,22] Therefore, researchers have determined the drag and lift coefficients of stiff-wing models as a function of the angle of attack to study the flight physics under a constant incident velocity.[3] These classical measurements are subsequently made more sophisticated by including the effects of aeroelastic performance[11,20] or studying the behavior of morphing wingtips.[14] However, we are interested in conducting an aerodynamic study of an aerial vehicle under steady load conditions without accounting for spanwise flexibility. To that end, we ignore chordwise wing deformation,[19] which is also responsible for the fact that the effective angle of attack can vary.[24] Thus, we use a wing model characterized by (1) a high stiffness and (2) a spanwise deformation.

The goal of this study is to analyze models with an imposed spanwise deformation with a low chord-based Reynolds number, $Re = 20 \times 10^3$ (see its definition below), and on a wing model with a relatively small semi-aspect (semi span length to chord) ratio, $sAR = 2$. The motivation for this study lies in the advent of increasingly lighter airfoil materials causing considerable spanwise deformations. We used a low Reynolds number because aerodynamics in this range has not yet been explored in detail[41] for applications such as micro air or unmanned aerial vehicles (MAVs and UAVs) or aerial vehicles for space missions in the stratosphere.[42,46,47] Low aspect ratio wings are essential in these applications. In addition, to apply computer-aided design, it is necessary to solve the problem of spanwise wing deformation when the wing is under distributed aerodynamic load.[24,26,51,53]

We used the NACA 0012 profile for our study.[12,45] The slope of the lift with the angle of attack of this slender airfoil presents a non-linearity.[5,32,44,50] Thus, this airfoil for a Reynolds number between values close to $Re = 20 \times 10^3$ and less than 80×10^3 shows a near-zero and negative lift for values of the angle of attack between 0° and 2°.[47] This dead zone has been reported on a few occasions by various authors.[32,35,39] The most plausible explanation for the appearance of this zone with a negative lift is due to a two-dimensional (2D) effect in which there is a pre-alignment of the flow at the leading edge.[1]

Concerning the effect of spanwise deformation on the lift coefficient and the trailing vortex, we will focus on the former aspect and find that numerous data confirm an *effective* increase in lift with deformation before stall. However, other studies report higher lift coefficients in the non-deformed (ND) wing models for small values of the angle of attack.[11,26,53] We also show this result in our experimental study, thus confirming the same performance. On the other hand, the study of wingtip vortices is of great interest in aerodynamics. Researchers use three theoretical models with which one can obtain their parametric characterization from experiments:[16] Lamb-Oseen, Batchelor,[6] and Moore and Saffman.[31] These turbulent wake structures have shown to be very stable and persistent over time, and numerous investigations try to understand their patterns downstream,[21] stability,[4,7,8,10,23] and how they can reduce their strength,[9,17,22,27,52] among other studies that concern about vortex wandering using NACA 0012 wing models.[15,18]

Several authors explain the generation of lift and its changes in value by changing flow patterns in a two-dimensional airfoil.[13,36,37,43] In this sense, Winslow *et al.* have schematically differentiated regions for Reynolds ranging between $Re = 20 \times 10^3$ and 50×10^3.[46] Thus, as the angle of attack increases, the laminar separation bubble (LSB) moves from being concentrated at the trailing edge to an intermediate zone of the airfoil located further upstream, i.e., the separation point moves closer to the leading edge, thus increasing the size of the shear layer. There are other studies in which this range of Reynolds numbers cited above extends up to $Re = 60 \times 10^3$. In addition, the lift increases with the angle of attack and Reynolds number.[49]

Prandtl's original lifting line theory[34] provides another relevant aspect in the interplay of the circulation generated in the airfoil and the wingtip vortices. Specifically, we refer to the combination of the flow patterns formed in the areas adjacent to the separation bubble and the wingtip vortices during their roll-up process.[40] This interaction can produce the disappearance of the vortex lift for very low aspect ratios.[33] For this reason, many authors are making a significant effort to understand the physical mechanism of this interaction for different aspect ratios and low to moderate Reynolds numbers.[28,38] Finally, it is interesting to remark how force measurement and velocity measurements can be related using the idea about the circulation that Xu *et al.*[48] very recently exposed. They obtained a constant, k, to relate the circulation contained in the trailing vortex Γ_{vortex}, which can be derived from velocity measurements on a plane perpendicular to the movement, and the wing circulation computed throughout the wing $\bar{\Gamma}_{wing}$, directly obtained from the force measurements. These authors estimated this constant for several numerical simulations of low aspect ratio hydrofoils with different geometries and conditions, thus providing a constant value k ranging between 0.9 and 1.0. Xu *et al.*[48] reported this last interval for any semi-aspect ratio sAR and $Re = 600 \times 10^3$. Another finding of our study results in the validity of the k-range for smaller Reynolds number.

This paper is organized as follows: Section II contains details of the experimental procedure of force and velocity, including the methodology for post-processing the velocity and the theoretical model used. Section III describes the main force results and the influence of the wing deformation on the lift coefficient. Section IV analyzes the impact of the wing deformation on the velocity measurements and circulation. Section V is devoted to the conclusions of this work.

II. EXPERIMENTAL SETUP AND TECHNIQUES

We performed the experiments using a towing tank at the Laboratory of Aero-Hydrodynamics of the University of Málaga. The towing tank is enclosed by transparent 25-mm thick perspex walls, allowing flow visualizations. The tank measures 10 m in length and features a cross-sectional dimension of $0.5 \times 0.5\ m^2$. We installed a laser sheet perpendicular to a wing moving at a constant speed in the z-direction. Figure 1 illustrates a three-dimensional (3D) depiction of the experimental setup with the wing model moving from right to left.

Three rectangular wing models with the same NACA 0012 airfoil profile and semi-aspect ratio of $sAR = 2$ were tested. This symmetrical wing section, chosen with a chord of $c = 0.1$ m and a semi spanwise length of $l = 0.2$ m, presents a maximum thickness equivalent to 12% of the chord. Each of the three tested NACA 0012 wing profiles corresponds to a different level of deformation in the spanwise direction. These rigid models have imposed deformations to replicate the ones measured experimentally in Farnsworth *et al.*[20] Specifically, they corresponded to tip deflections of $\delta = 0\%$ (non-deformed, ND), $\delta = 2\%$ (intermediate deformation, ID), and $\delta = 4.5\%$ (large deformation, LD) of the wingspan (originally obtained from a NACA 0018 profile with $sAR = 6$ and $Re = 230 \times 10^3$). While the intermediate deformation profile corresponds to the deflection experienced by the wing for an angle of attack of $\alpha = 5°$, the large deformation corresponds to $\alpha = 10°$.[20] Figure 2 reproduces the profiles on the spanwise direction of the non-deformed profile with the two levels of deformations. It is noteworthy to specify that for the deformed cases, the length corresponds to the projection of the wing on the *x-axis*, being the total curvilinear wing length slightly greater.

We performed all the experiments at a chord-based Reynolds number of $Re = W_\infty c/\nu = 20 \times 10^3$. This constant value is achieved by adjusting the forward velocity of the wing profile W_∞, considering the water temperature, T, and its corresponding kinematic viscosity $\nu(T)$. The velocity is then set to a constant value controlled by an electric motor, which provides a maximum velocity of 400 mm/s with an error lower than 0.5%. The electric motor is controlled by a laptop with feedback by means of an encoder, and the control of the acceleration from rest and the final position of the model was set using Matlab® through the USB port. We set the angle of attack for the wing models using a high precision rotating platform attached to the moving structure on the towing tank. We did not observe any relevant towing tank blockage effects since it had a maximum value of 1.9% for $sAR = 2$.

The proposed experimental setup aims to obtain values for two sets of variables: the hydrodynamic forces exerted on the wing profile and the velocity field of the trailing vortex. Finally, to check the repeatability of the experimental setup and to obtain the standard deviation of lift with the level of wing deformation, each experiment was repeated 3 times with unchanged experimental conditions. Thus, all the force and velocity results shown in the paper represent the averaged value of these three tests. The details relative to both variables are exposed, respectively, in Secs. II A and II B.

A. Force measurements

We measured the hydrodynamic forces applied on the wing profile during its translation along the towing tank with the precise six-axis force/torque sensor ATI FTD-Nano17 SI-12-0.12 sensor of accuracy ± 0.003 N. This load cell, mounted on the mobile platform

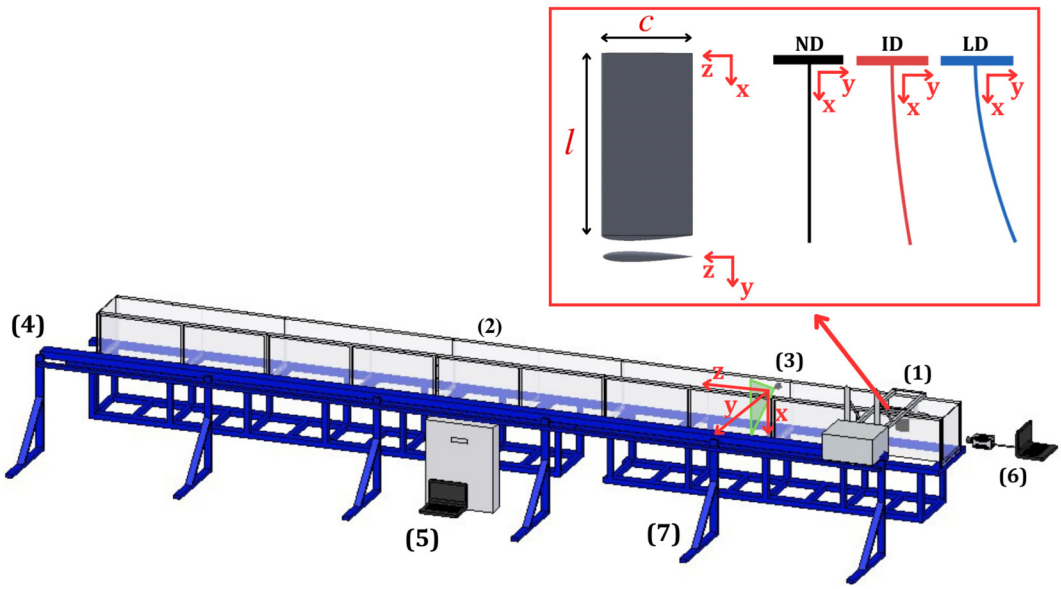

FIG. 1. Three-dimensional schematic representation of the experimental setup: NACA 0012 wing with a semi-aspect ratio $sAR = 2$ mounted on a support moving in the axial coordinate z from right to left (1), perspex channel (2), laser light plane (3), rail track (4), computer that regulates the velocity control of the guide rail (5), high speed camera (6), and blue mounting structure (7).[21] The top box contains a schematic of the NACA0012 models: non-deformed (ND, $\delta = 0\%$), intermediate deformation (ID, $\delta = 2\%$), and large deformation (LD, $\delta = 4.5\%$).

on the towing tank, is connected to each of the tested wing profiles through the high-precision rotating platform. We ensured the orientation of the wings using a digital inclinometer with an accuracy of 0.1°.

We might be aware of some considerations to calculate the lift and drag coefficients from force measurements. Given that the z-axis of the transducer aligns with the direction of gravity, hydrodynamic forces exclusively act within the (x, y)-plane. The force sensor was aligned with the direction of the movement, establishing a global coordinate system in which the lift force can be directly obtained. The global lift component F_L is set perpendicularly to the free-stream velocity W_∞. In order to compute the force using the local coordinate system aligned with the wing chord, we applied the following transformation:

$$F_L = F_{x'} \sin(\alpha) + F_{y'} \cos(\alpha). \tag{1}$$

It is essential to consider the eventual offset of the force measurements, which has to be subtracted from the force signals to obtain the hydrodynamic forces over the airfoil. Then, we computed the non-dimensional lift coefficient using the following expression:

$$C_L = \frac{2F_L}{\rho W_\infty^2 A}, \tag{2}$$

where ρ is the water density at the corresponding temperature, W_∞ is the translation velocity of the wing profile, and A is the planform area of the model, $A = l \cdot c$.

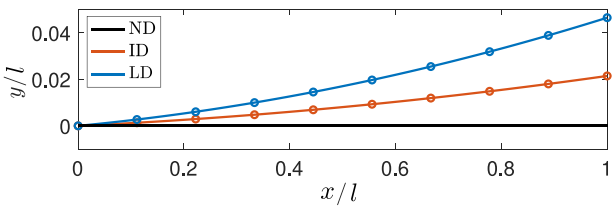

FIG. 2. Non-dimensional deflection levels along the spanwise direction considered in this study, corresponding to deformations observed from Farnsworth *et al.*:[20] non-deformed (ND, $\delta = 0\%$), intermediate deformation (ID, $\delta = 2\%$), and large deformation (LD, $\delta = 4.5\%$).

B. Velocity measurements

We measured velocity fields belonging to trailing vortices using the 2D-PIV technique. This technique captures velocity information of the whole flow fields in a fraction of a second using two consecutive images from the illuminated tracer particles in the laser plane. The laser sheet is positioned in a fixed position perpendicular to the axial axis (z), illuminating an (x,y)-plane, enabling the reconstruction of both azimuthal and radial velocity components in the wake alongside the axial coordinate. Note that the dimensional axial position, z, is measured from the laser sheet to the trailing edge of the wing model.

The 2D-PIV system consists of two main components: (1) a laser sheet that is less than 1 mm thick in the measurement section obtained using one green laser source of 1 W (Microvec model SM-SEMI-1W) in conjunction with a set of lenses (cylindrical lens of −6.25 mm focal length) and a mirror that was installed in front of the laser plane to obtain a better illumination sheet, (2) a high-speed monochrome camera Phantom model CINEMAG-II v611 with a Tamron lens (SP 70–200 mm f/2.8) at a rate of 125 fps, equivalent to a time interval between images of $\Delta t = 8$ ms. This experimental setup allowed us to obtain the wing wake evolution over a distance of 20c from the motion onset. We collected velocity measurements for angles of attack $\alpha = 4$–$8°$.

As tracer particles to perform 2D-PIV, we used glass silver-coated spheres of 10 μm (HGS-10 from Dantec). These seeding particles are neutrally buoyant in water, thus minimizing their relative motion to the water flow due to gravity and centrifugal accelerations. The calibration process for the 2D-PIV imaging setup relies on capturing images of a planar calibration target positioned parallel to the light sheet plane. This calibration target comprises a grid of dot markers equally spaced at 10 mm intervals, facilitating straightforward detection using simple image processing techniques.

The PIV algorithm to extract the velocity fields from the images was DPIVSoft.[2,30] This program employs a double pass PIV method with a window deformation of 32×32 pixels. Therefore, we obtained a grid containing horizontal and vertical velocity components (u, v) for each snapshot pair. These velocity profiles were later post-processed to characterize the wingtip vortices.

In addition, to verify the absence of systematic errors, we leveraged the software developed in Mendes *et al.*[29] to generate synthetic images emulating a q-vortex flow under our experimental conditions. These conditions encompassed such factors as maximum azimuthal velocity, particle size, particle density, and pixel-to-mm ratio. With this technique, we verified that the estimated velocity errors remained below 1% of its magnitude.

C. Velocity fields post-processing

2D-PIV measurements provide a grid of velocity data for each measured plane using a global reference point. However, we are interested in analyzing these data sets for wingtip vortices. Wingtip vortices are disturbed by turbulence, causing an unpredictable shift in their center position known as meandering.[15,18] Even though this phenomenon is not very pronounced due to the low turbulence in the towing tank, it is necessary to identify the vortex center and establish it as the local center for our coordinate system to allow comparing velocity fields across different axial distances.

To determine the vortex center, we used a two-step approach to approximate its position first and to refine the approximation later. We computed the first step following the gradient of the stream function, which inherently points toward the vortex center. This direction, denoted β, can be calculated at a given point (i, j) as

$$\beta_{i,j} = \tan^{-1}(v_{y_{i,j}}, v_{x_{i,j}}) + \pi/2. \tag{3}$$

From an initial guess point, incremental movements in the β direction ultimately converge toward a point close to the vortex center. This first procedure is very convenient for experimental data due to its robustness against spurious values of the velocity fields.

The second step applied a more precise method to refine the vortex center estimation. This method is based on calculating the maximum vorticity position and has proven quite efficient.[21] Specifically, the vorticity field is approximated by a two-dimensional second-order polynomial function in the nearest points to the first center estimation. The polynomial used has the following form, presenting a total of six adjustable coefficients:

$$P(x, y) = a_1 + a_2x^2 + a_3y^2 + a_4xy + a_5x + a_6y. \tag{4}$$

Since the vorticity peak occurs at the vortex center, its coordinates can be calculated at the sub-grid interpolation level as follows:

$$x_{vc} = \frac{a_4a_6 - 2a_3a_5}{4a_2a_3 - a_4^2}, \quad y_{vc} = \frac{a_4a_5 - 2a_2a_6}{4a_2a_3 - a_4^2}. \tag{5}$$

After the computation of the vortex center (x_{vc}, y_{vc}), all the velocity data are re-centered and interpolated accordingly. Due to the pronounced axial symmetry exhibited by wingtip vortices, it is advantageous to analyze them within the framework centered on the vortex and using cylindrical polar coordinates (r, θ) for each z measurement plane with velocity components (v_r, v_θ), respectively.

D. Theoretical models

One of the earliest theoretical models developed to describe the behavior of trailing vortices was formulated by Batchelor.[6] This model assumes axial symmetry in the vortex flow and addresses the Navier–Stokes equations in cylindrical polar coordinates (r, θ, z), with velocity components (v_r, v_θ, v_z). A boundary-layer-type approximation is applied, considering gradients in the axial direction much smaller than those in the radial direction $(\partial/\partial z \ll \partial/\partial r)$, while radial velocity is negligible compared to the axial component $(v_r \ll v_z)$. Simultaneously, the theoretical model considered the axial velocity defect (or excess) much lower than the free-stream velocity $(|v_z - W_\infty| \ll W_\infty)$. The resulting linearized parabolic equations are solved incorporating a boundary condition stating that in the far field, the axial velocity component approaches the flight speed and the tangential velocity takes the form of a potential vortex $(rv \to constant \equiv \Gamma_{core}/(2\pi)$ as $r \to \infty$, being Γ_{core} the vortex core circulation).[16] This results in zero radial velocity

$$v_r(r, z) = 0, \tag{6}$$

and the following expression for the azimuthal velocity component:

$$v_\theta(r, z) = \frac{\Gamma_{core}}{2\pi r}\left[1 - e^{-W_\infty r^2/(4\nu z)}\right]. \tag{7}$$

The axial velocity component will not be considered, as our experimental data has been acquired using the 2D-PIV technique, neglecting the out-of-plane velocity component.[21]

For a more comprehensive understanding of these vortices and to facilitate comparisons with other research studies, it is advantageous to analyze them using dimensionless variables based on the chord length c and the free-stream velocity W_∞

$$\bar{v}_\theta = v_\theta/W_\infty, \tag{8}$$

$$\bar{r} = r/c, \tag{9}$$

$$\bar{z} = z/c. \tag{10}$$

The use of these non-dimensional variables results in the following dimensionless expression for the azimuthal velocity in the Batchelor's model:

$$\bar{v}_\theta(\bar{r}, \bar{z}) = \frac{S}{\bar{r}}(1 - e^{\eta}), \tag{11}$$

where

$$S = \frac{\Gamma_{core}}{2\pi c W_\infty}, \tag{12}$$

$$\eta = -\frac{\bar{r}^2 Re}{4(\bar{z} - \bar{z}_0)}. \tag{13}$$

As del Pino *et al.*[16] pointed out, the axial vortex origin in the self-similar solution proposed by Batchelor is not well defined. To address this issue, an additional free parameter $\bar{z}_0$ has been added to the model. This parameter represents a virtual origin of the vortex different from the wingtip and improves considerably the fitting of the theoretical models with the experimental data.

The model proposed by Moore and Saffman[31] also incorporates the same boundary-layer-type and small axial velocity defect approximations as Batchelor's model. However, it uses a more realistic boundary condition for the tangential velocity as $\bar{r} \to \infty$, taking into consideration the roll-up process of the vortex sheet, resulting in a more realistic solution for the flow outside the viscous core. In this model, it is assumed that the vortex sheet is generated by wings with a circulation distribution across the wingspan $\Gamma(x) \sim x^{1-n}$, where $0 < n < 1$. In non-dimensional terms and with the inclusion of the free parameter z_0, the Moore and Saffman solution for azimuthal velocity can be expressed as

$$\bar{v}_\theta(\bar{r}, \bar{z}) = \frac{bRe^{n/2}}{(\bar{z} - \bar{z}_0)^{n/2}} V_n(\eta). \tag{14}$$

Here, b is a non-dimensional constant related to the vortex circulation, $V_n(\eta)$ is a function dependent on the gamma function and the hypergeometric function of the first kind, and n, the parameter defined by the wing circulation distribution, determines the vortex decay rate as $\bar{v}_\theta \to b\bar{r}^{-n}$ as $\bar{r} \to \infty$.

III. FORCE RESULTS

A. Validation

One of the defining properties of any wing model is its lift coefficient. The calculation of the lift coefficient for NACA 0012 profiles at low Reynolds numbers is not trivial due to the non-linearities present for small angles of attack. This subtle phenomenon has already been reported[1,32,35,39,49] and has been comprehensively studied. Additionally, as discussed extensively by Tank *et al.*,[39] there are some discrepancies in the results since they are extraordinarily sensitive to small changes in geometry and the environment. Nevertheless, we use the previous work of Ohtake *et al.*[32] and Yasuda *et al.*[49] to validate our forces measurements. Figure 3 represents the measured lift coefficient for a non-deformed model at $Re = 20 \times 10^3$ and semi-aspect ratio $sAR = 2$ for different angles of attack together with the results obtained from the literature. The values are very similar to Ohtake *et al.*[32] from $\alpha = 0$–7° and more similar to Yasuda *et al.*[49] for angles $\alpha > 7^\circ$. Note that even though Yasuda *et al.*[49] and Ohtake *et al.*[32] are using three-dimensional models with semi-aspect ratio $sAR = 2$, their experimental setup is different. The models of Yasuda *et al.*[49] are indeed measurements of a three-dimensional model, whereas the model used in Ohtake *et al.*[32] has the same height as the tunnel section, thus acting as a (airfoil) 2D model. There are also multiple pieces of literature about the modification for low aspect ratio foils and 3D effect; see, e.g., Hoerner.[25] More importantly than the exact value (due to the above-mentioned possible discrepancies in the exact values), the results match the same characteristics as the results exposed by Ohtake *et al.*[32] First, there is a small region about 0–3° with a strong non-linearity, including an almost zero lift value for an angle of attack $\alpha = 1^\circ$. Then, a second region appears between $\alpha = 3^\circ$ and $\alpha = 7^\circ$ with a strong C_L slope and, finally, the third area forms at $\alpha > 7^\circ$ with a middle slope region (region names were maintained from Ohtake *et al.*[32] for clarity).

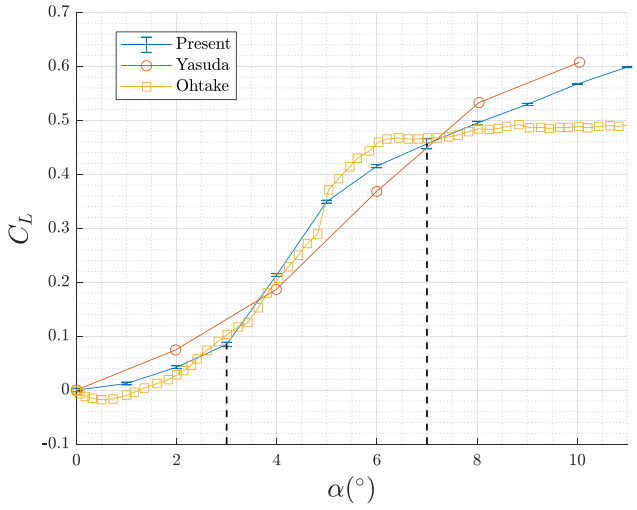

FIG. 3. Lift coefficient vs angle of attack. Results from our study, Yasuda *et al.*[49] and Ohtake *et al.*[32]

B. Influence of the deformation on the lift coefficient

In this paper, we aim to raise the question of how the spanwise deformation affects an already complicated behavior of the lift coefficient on the NACA 0012 profile wings. The measured lift coefficients of the three wing models (non-deformed, intermediate deformation and large deformation) are represented as a function of the angle of attack α in Fig. 4. First of all, we focus our attention on the division of the three distinctive regions: non-linear $\alpha = 0$–3°, large C_L slope $\alpha = 3$–7°, and intermediate slope $\alpha > 7^\circ$. The three zones are clearly defined not only for the non-deformed case but also for the deformed ones.

Analyzing each zone in detail, we observe that the lift coefficient diminishes with deformation in the non-linear region. Also, we find

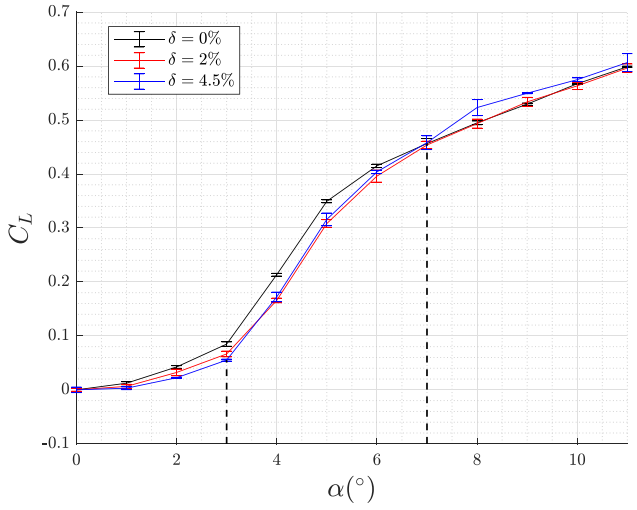

FIG. 4. Lift coefficient variation vs the angle of attack for cases with $sAR = 2$ and $Re = 20 \times 10^3$ for three levels of deformation.

that C_L is approximately zero at $\alpha = 1°$ for all the deformations. These results also confirm this phenomenon being a purely 2D effect.[1] The large C_L slope regions present a slope very similar in the deformed and non-deformed wings up to $\alpha = 6°$, being the values of CL smaller for the deformed wings since they were smaller at $\alpha = 3°$. At $\alpha = 6°$, the C_L slope changes differently for the deformed wings, and the differences on C_L are lower as we approach the third region. At $\alpha = 7°$, we enter the middle C_L slope region, and the changes in the behavior of the deformed wings are evident. First, we can appreciate a noticeable difference between the intermediate and large deformation wings for $\alpha > 7°$. The intermediate deformation mimics the non-deformed model, showing negligible differences in the C_L, whereas for $\alpha < 7°$, these two levels of deformation exhibit similar behavior. Therefore, a larger deformation is required to observe a significant effect in C_L for higher angles of attack. Second, we noticed that for $\alpha > 7°$, forcing a big enough deformation increases the C_L contrary to the observations made for smaller angles of attack.

To explain the results of $C_L(\alpha)$ for the non-deformed case, we can analyze the pressure profiles at different angles of attack over NACA 0012 airfoils presented by Anyoji *et al.*[5] and Tsuchiya *et al.*,[44] at $Re = 20 \times 10^3$ and $Re = 25 \times 10^3$, respectively. In these Reynolds numbers, from $\alpha = 3°$ to $\alpha = 7°$, the flow evolves from not presenting an LSB to showing a larger LSB, which shortens considerably as α is increased. This range of angles of attack corresponds to that in which our measured C_L increases sharply, suggesting a change in the flow regime as the causing mechanism for this effect. For the evidence given above, a plausible explanation of how the LD case has larger values of C_L than the ND case for $\alpha > 7°$ is that the spanwise deformation wing remains with larger LSB at higher angles of attack. It is also evident that the presence of a critical spanwise deformation since ID data follows ND findings.

IV. VELOCITY RESULTS

A. Validation

To validate our 2D-PIV measurements, we first corroborate the general structure and characteristics of wingtip vortices observed in our experimental data. Notably, one prominent attribute of these vortices is the pronounced axial symmetry they exhibit once the roll-up process of the vorticity sheet has been finalized. This symmetry is appreciable in Fig. 5, which displays flow velocity (in arrows) together with vorticity contours at $z/c = 7$. This plane was selected as an example without any particular reason, considering that symmetry continues as the vortex evolves in the z direction.

Figure 6(a) represents experimental dimensionless v_θ in solid lines at $z/c = 10$. Note that due to the symmetry of the vortices, the azimuthal component of the velocity is averaged for every angular position, obtaining a representative value of v_θ for each radial position. Figure 6(a) also illustrates the core radius r_{core} position defined as the radial distance of the azimuthal velocity peak. In addition, Fig. 6(a) also represents, together with the experimental results, the values obtained with the Moore and Saffman[31] and Batchelor[6] models with their corresponding adjusted parameters. Moore and Saffman[31] model is able to reproduce very accurately the velocity results of this experiment. Figure 6(b) represents the dimensionless v_θ for $z/c = 20$. The form of the radial v_θ profiles is similar for all z distances. However, the maximum value of v_θ is decreasing, and the radius of the core is increasing along the z-axis as expected in trailing vortices. Also, at the outer regions of the vortex ($r/c \gtrsim 0.2$), the velocity profiles overlap for all the axial distances studied, as the velocity induced by a vortex core in the far field is similar to the one induced by a singular point with the same total circulation.

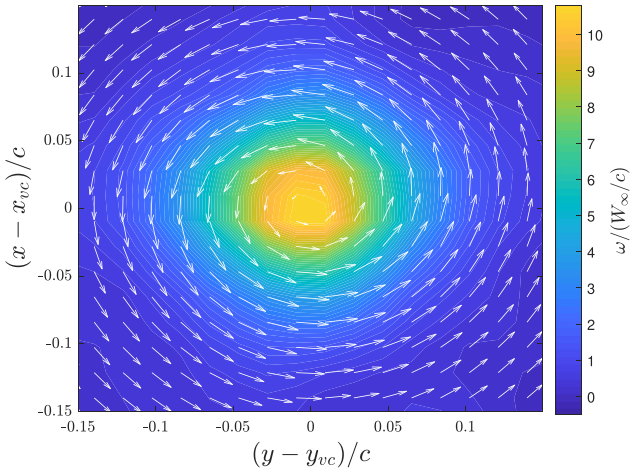

FIG. 5. Results for a non-deformed wing at $\alpha = 8°$: Experimental velocity and dimensionless vorticity fields at $z/c = 7$.

Finally, we compare our results for the non-deformed wing with the ones obtained by del Pino *et al.*[16] In this article, as in our case, the 2D-PIV technique was used to measure the velocity fields in the wake generated by wing models with a NACA 0012 profile and $sAR = 2$ at $Re = 20 \times 10^3$. Therefore, we have computed the parameters for the theoretical models for our results and compared them with their results. Table I contains the parameters for the Moore and Saffman[31] model for both studies. The results show good agreement despite the different techniques used to compute the velocity and the difference in the angle of attack. del Pino *et al.*[16] measurements were taken using a large water tunnel, whereas the present study uses a towing tank. The angles of attack were $\alpha = 6$–9–$12°$ in del Pino *et al.*,[16] and the theoretical parameters computed with the average and our results present the averaged values over $\alpha = 6$–7–$8°$ since S grows linearly with the angle of attack.

B. Influence of wing deformation in the wingtip vortex general structure and axisymmetry

After briefly discussing the well-known features of wingtip vortices, we shift our attention to the influence of the spanwise wing deformation. The vortex symmetry remains unaltered despite the level of wing deformation. This behavior is illustrated in Fig. 7 with velocity and vorticity fields at $z/c = 7$. However, it remains unaltered for any other z value after the roll-up process. This characteristic is essential for further analysis and validates the application of azimuthal averaging some properties, even in cases featuring wing deformation.

The most considerable effect of the deformation on v_θ is the change of its magnitude [compare Fig. 8(a) with Fig. 6(a)]. No substantial change is appreciated in the position of the vortex core radius. Two representative examples of v_θ profiles have been chosen at $z/c = 10$, Fig. 8(a), and $z/c = 20$, Fig. 8(b), but its structure is maintained for any other z position along the vortex.

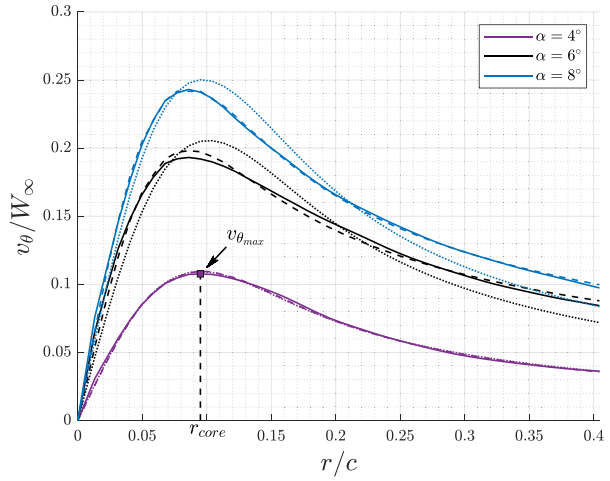

(a)

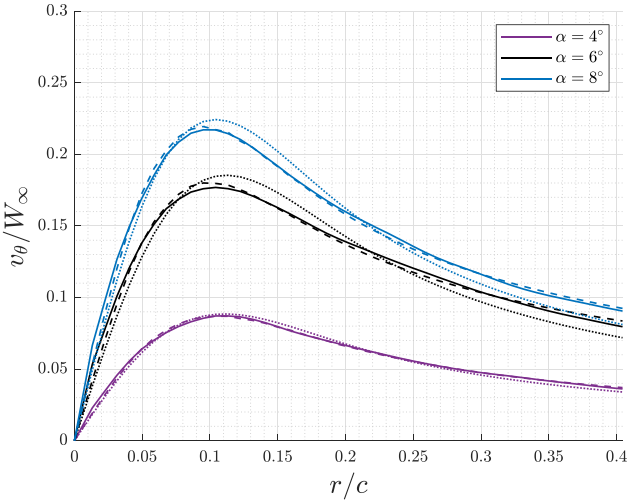

(b)

FIG. 6. v_θ/W_∞ for a non-deformed model at a plane (a) $z/c = 10$ and (b) $z/c = 20$. Solid lines represent experimental measurements, dashed lines represent the Moore and Saffman[31] model, and dotted lines represent the Batchelor[6] model.

Focusing our attention on the theoretical models, we first analyze the S parameter of the Batchelor[6] model and the b parameter from the Moore and Saffman[31] model that is related to the vortex circulation. Figures 9 and 10 present these parameters for different angles of attack

TABLE I. Comparison between the parameters of the Moore and Saffman[31] model for the present study and del Pino *et al.*[16]

Parameter	del Pino *et al.*[16]	Present
b/α	7.5×10^{-3}	7.3×10^{-3}
n	0.54	0.69
$\bar{z}_{0MS}$	-9.4×10^{-4}	-5×10^{-4}

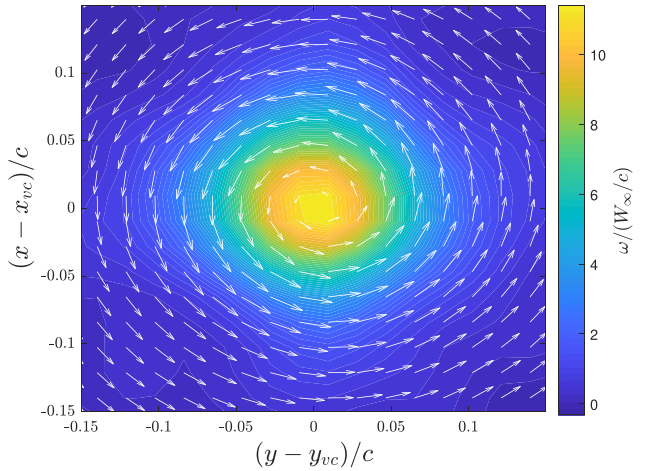

FIG. 7. Results for a deformed wing with $\delta = 4.5\%$ at $\alpha = 8°$: Experimental velocity and dimensionless vorticity fields at $z/c = 7$.

and for the non-deformed and large deformation models. We can observe how for both parameters the deformed model shows smaller values for angles of attack $\alpha = 4$–$5°$, then they almost coincide for $\alpha = 6°$ and then they present a change in the trend for values $\alpha = 7°$, showing the deformed model higher values.

The n parameter, represented in Fig. 10, describes the decay rate of the azimuthal velocity with the radial distance ($v_\theta \sim r^{-n}$). Our results show that this parameter does not seem to be dependent on wing deformation. For $\alpha \geq 6°$, it remains constant at a value of approximately 0.7. However, below 6°, n increases and at $\alpha = 4°$, it is almost equal to 1, which represents the radial decay of a potential vortex. This characteristic explains why Batchelor's model fits the experimental results better at $\alpha = 4°$; see again Figs. 6 and 8.

C. Circulation and effect of wing deformation on the circulation

Due to the importance of the circulation in further analysis of the vortex, we analyze its evolution in a separate subsection. Circulation, $\Gamma(r)$, is defined as the circulation around a circular path of radius r, centered on the vortex and determined directly through the line integral of the velocity field ($\Gamma = \oint \vec{v} \cdot \vec{dl}$). Figure 11 shows the value of $\Gamma(r)$ averaged for any z plane for non-deformed (in solid lines) and large deformation (in dashed lines) wings for different angles of attack. The circulation is always increasing as we move away from the vortex core as expected, showing two clear regions: one with a stronger slope at the vortex core and another one where its increase is less pronounced or becomes even constant depending on the cases outside the core.

This circulation behavior is an expected result that is typical in vortex analysis. However, the novelty elucidated here is the influence of the deformation on the circulation. The deformation decreases the circulation for small angles of attack and increases the circulation for larger angles of attack. The change in this behavior is appreciable between $\alpha = 6$–$7°$ as it was also evident in the analysis of the b and S parameters; see Figs. 9 and 10. This change also coincides with the change in the trend displayed on the lift coefficient in Fig. 4,

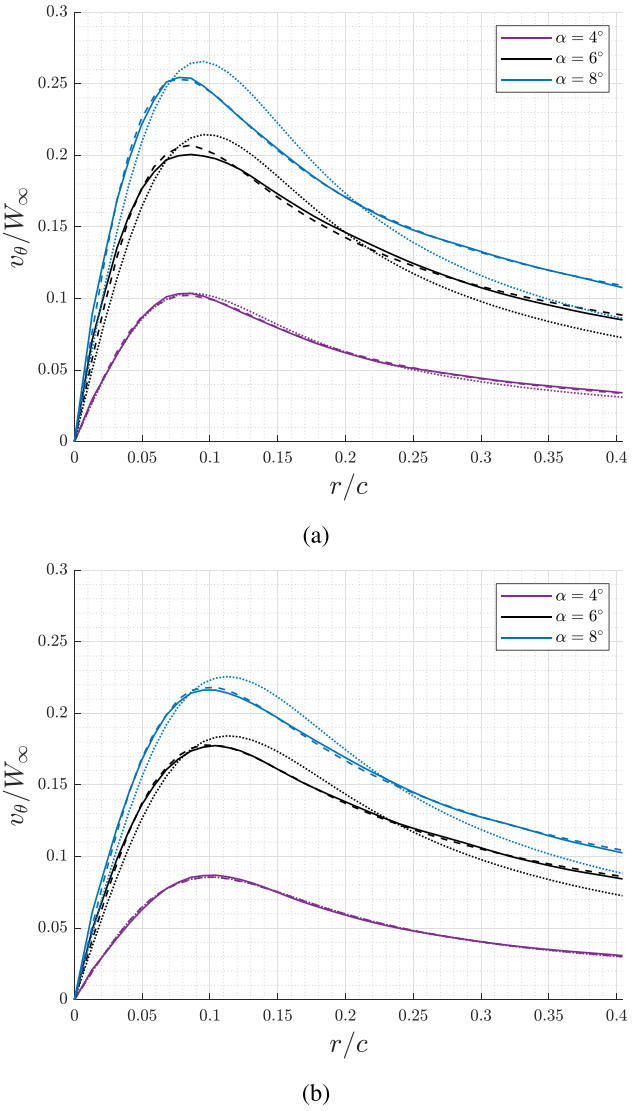

FIG. 8. v_θ/W_∞ for a deformed model with $\delta = 4.5\%$ at a plane (a) $z/c = 10$ and (b) $z/c = 20$. Solid lines represent experimental measurements, dashed lines represent the Moore and Saffman[31] model, and dotted lines represent the Batchelor[6] model.

comparing deformed and non-deformed models. The connection between the circulation and the lift coefficient will be further elaborated in Sec. IV D.

Now, we focus our attention on the evolution of the circulation along the z-axis. It is well known that the vortex intensity decays in the downstream direction. Therefore, the evolution of $v_{\theta_{max}}$ along the z axis (not shown) gradually decreases after the roll-up process. However, note that after the roll-up process, the core circulation is preserved, due to the fact that the core radius increases at the same rate that the peak azimuthal velocity decreases ($r_0 v_{\theta_{max}} = cte$). See Fig. 12 for the downstream evolution of core circulation.

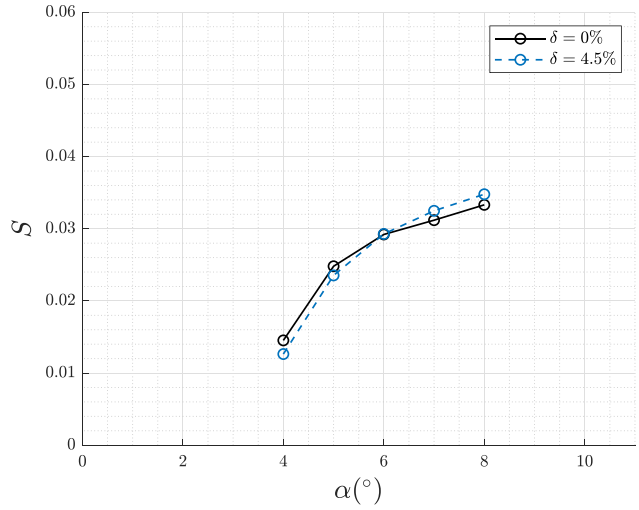

FIG. 9. Parameter S of the Batchelor[6] model vs the angle of attack for non-deformed wing (solid line) and deformed wing with $\delta = 4.5\%$ (dashed lines).

Wing deformation maintains similar patterns for the evolution of circulation as observed in Fig. 12 dashed lines. $v_{\theta max}$ and core radius (not shown) also show similar behavior to the non-deformed cases.

D. Wingtip vortex circulation and its relationship with wing hydrodynamic forces and spanwise circulation distribution

Wing circulation along its span direction can be computed by applying the Kutta–Joukowski theorem and integrating along the wing span as

$$\bar{\Gamma}_{wing} = \frac{1}{2} C_L W_\infty c. \tag{15}$$

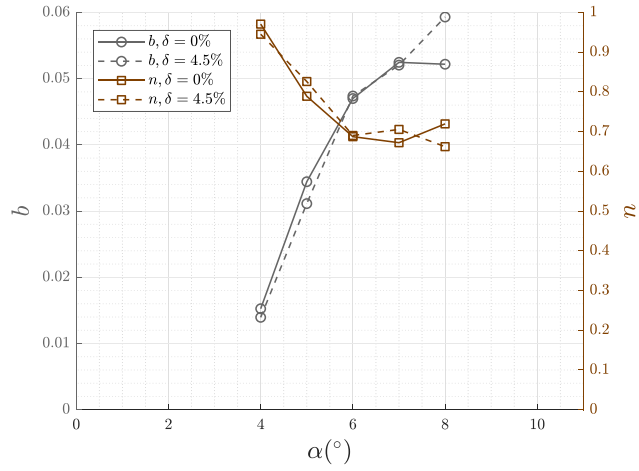

FIG. 10. Parameters b and n of the Moore and Saffman[31] model vs the angle of attack for non-deformed wing (solid line) and deformed wing with $\delta = 4.5\%$ (dashed lines).

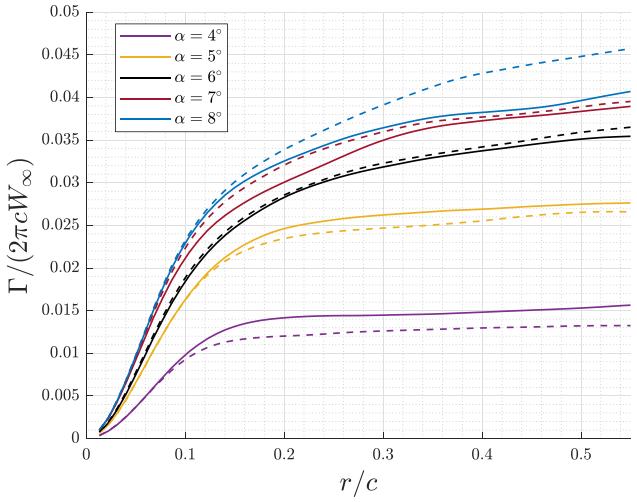

FIG. 11. Dimensionless circulation averaged for every $z \geq 5c$ respect to the dimensionless radial coordinate for 5 different angles of attack. Solid lines represent non-deformed wings and dashed lines represent deformed wings with $\delta = 4.5\%$.

Therefore, the average spanwise circulation around the wing is directly computed from the lift coefficient. The spanwise circulation decreases from a maximum to zero in the wingtips, and this variation can be understood as the mechanism by which the streamwise circulation is generated and shed into the wake. Since most of the vorticity shed by the wing is rolled up in the wingtip vortex, Xu *et al.*[48] very recently developed a method to estimate the circulation contained in the vortex from the hydrofoil load. This vortex circulation, Γ_{vortex}, is measured in a downstream plane perpendicular to the flow direction and can be computed directly from velocity measurements. Both circulations can be related to the following formula:

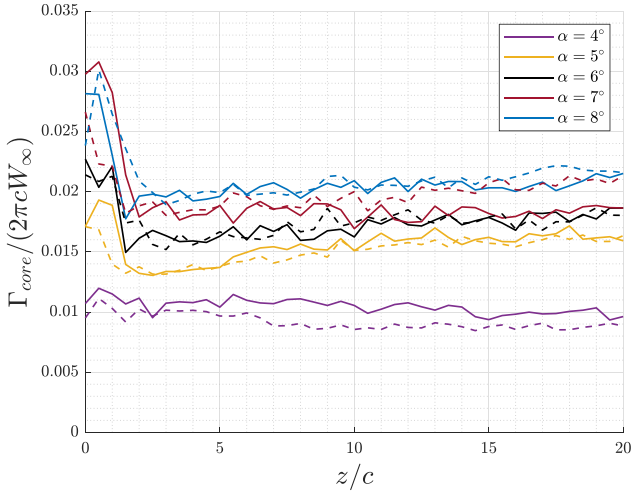

FIG. 12. Experimental axial profile of the dimensionless core circulation vs dimensionless span direction for different angles of attack. Solid lines represent non-deformed wings and dashed lines represent deformed wings with $\delta = 4.5\%$.

$$\Gamma_{vortex} = k\bar{\Gamma}_{wing} = \frac{1}{2}kC_L W_\infty c. \tag{16}$$

They estimate a value of k between 0.9 and 1 based on several numerical simulations of low aspect ratio hydrofoils with different geometries and conditions. We refer to the original paper Xu *et al.*[48] for further details about how to obtain this relationship.

In our study, $\bar{\Gamma}_{wing}$ is computed from the C_L measurements and Γ_{vortex} from the 2D-PIV measurements. Γ_{vortex} refers to the total circulation contained in the vortex, that is, $\Gamma(r)$ measured at a radial distance where the vortex flow is irrotational. Specifically, we have estimated $\Gamma_{vortex} \approx \Gamma(r/c = 0.4)$ and averaged it for all the axial distances $z/c \geq 5$, where the roll-up processed has finished. Note that, for $\alpha > 5°$, the flow is still not completely irrotational at $r/c = 0.4$. However, we have used $\Gamma(r/c = 0.4)$ to estimate the value of Γ_{vortex} since the non-averaged circulation measurements (not shown) do not show a clear tendency after that value, whereas up to $r/c = 0.4$, all experimental measurement displays a very small dispersion both between experiments and between z values.

$\bar{\Gamma}_{wing}$ can be easily computed from the lift coefficient, see Eq. (15). Therefore, we obtain the value of k as $\Gamma_{vortex}/\bar{\Gamma}_{wing}$ for each experiment. See Table II for the values of each magnitude for deformed and non-deformed wings for angles of attack $\alpha = 4°$, 6°, and 8°. All the k values for non-deformed models are in the range of $0.87 - 1.03$, displaying an excellent agreement with Xu *et al.*[48] proposed formula. Note also that for the non-deformed cases, this formula is still valid with slightly higher values of k, in the range of 0.94–1.07.

Last, as seen in Fig. 11, the circulation displayed a tendency change at $\alpha = 6$–$7°$ when comparing deformed and non-deformed cases. This change coincides also with the change in tendency displayed on the lift coefficient in Fig. 4. This coincidence should not be an unexpected result since the circulation and the lift coefficient are proportional as shown in Eq. (16). Figure 13 displays Γ_{vortex} to facilitate the visual comparison between circulation and the lift coefficient shown in Fig. 4 and the influence of the deformation in both.

V. CONCLUSIONS

We have analyzed the influence of the spanwise wing deformation on the wingtip vortex using a towing tank for $Re = 20 \times 10^3$ using models with a semi-aspect ratio of $sAR = 2$ and three levels of

TABLE II. Comparison between Γ_{vortex}, $\bar{\Gamma}_{wing}$, and k values for deformed and non-deformed wings.

Deformation	α	$\Gamma_{vortex}/(2\pi W_\infty c)$	$\bar{\Gamma}_{wing}/(2\pi W_\infty c)$	k
$\delta = 0\%$	4°	0.0148	0.0170	0.87
	5°	0.0269	0.0278	0.97
	6°	0.0338	0.0330	1.02
	7°	0.0373	0.0363	1.03
	8°	0.0383	0.0394	0.97
$\delta = 4.5\%$	4°	0.0130	0.0137	0.94
	5°	0.0256	0.0251	1.02
	6°	0.0343	0.0321	1.07
	7°	0.0377	0.0365	1.03
	8°	0.0429	0.0416	1.03

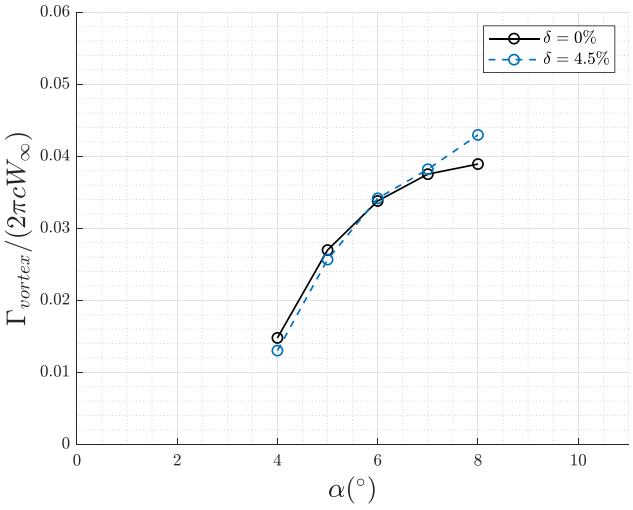

FIG. 13. Dimensionless Γ_{vortex} vs the angle of attack for non-deformed wings (solid line) and deformed wing with $\delta = 4.5\%$ (in dashed lines).

spanwise deformation: non-deformed (ND), tip deflection of $\delta = 2\%$ (ID), and tip deflection of $\delta = 4.5\%$ (LD).

2D-PIV measurements were performed to analyze the wingtip vortex behind the wing, and these data, combined with force measurements, provided enough information to present a general analysis of the impact of deformation on a wingtip vortex and the main aerodynamic characteristics of the wing.

We have observed that the deformation does not alter the general structure of the vortex. Therefore, the theoretical model of Moore and Saffman[31] still accurately reproduces the velocity profiles when using the appropriate parameters.

Force measurements reveal three distinct zones in the range of angles of attack studied, each characterized by different lift slopes. These three zones are still appreciable for the deformed wings. For small angles of attack, even a (ID) deformation of 2% has a strong effect on the C_L. However, for $\alpha > 7^\circ$, a higher level of deformation (LD) is required to observe any change in the lift concerning the non-deformed wing. Additionally, one of the key results is that the deformation decreases the lift for $\alpha < 7^\circ$ with respect to the lift of non-deformed values and increases it for greater α. This change in tendency comparing deformed wings with non-deformed ones can also be observed in the circulation level being lower for deformed cases for $\alpha < 7^\circ$ but higher for greater α. This change in behavior can be explained using the relationship between the circulation over the wing due to lift vortex (obtained from C_L) and the circulation measured in a plane perpendicular to the movement (computed from 2D-PIV) presented by Xu *et al.*[48] Our data shows a strong alignment between the proposed relationship of these circulations even though we are in a value of Reynolds significantly smaller than theirs. Finally, this study shows that the relationship between circulation levels Γ_{vortex} and $\bar{\Gamma}_{wing}$ still holds for the deformed cases, having the deformation a subtle influence on the constant value, k, that relates both circulations.

In conclusion, the influence of the spanwise deformation is complex to analyze at low Reynolds numbers for a NACA 0012 wing model, and further detailed studies of flow patterns are required since the effect of the deformation varies with the angle of attack. The maximum tip deflection analyzed in this work corresponds to 4.5%, and we have shown that deformations of this order of magnitude already alter the lift and the wingtip vortex associated with the wing model for $sAR = 2$.

ACKNOWLEDGMENTS

This work was supported in part by the Ministerio de Ciencia e Innovación of Spain (Grant No. PID2021-124692OA-I00). We thank Full Professor Luis Parras for his fruitful discussions about the physics contained in this paper, and Kevin Hoff for his improvements in the English style.

AUTHOR DECLARATIONS

Conflict of Interest

The authors have no conflicts to disclose.

Author Contributions

Pedro Solis: Data curation (equal); Formal analysis (equal); Investigation (equal); Methodology (equal); Writing – original draft (equal); Writing – review & editing (equal). **Manuel Garrido-Martin:** Formal analysis (equal); Methodology (equal); Validation (equal); Writing – review & editing (equal). **Eduardo Duran:** Formal analysis (equal); Investigation (equal); Supervision (equal); Writing – review & editing (equal). **Paloma Gutierrez Castillo:** Conceptualization (equal); Formal analysis (equal); Funding acquisition (equal); Project administration (equal); Supervision (equal); Writing – review & editing (equal). **Carlos del Pino:** Conceptualization (equal); Formal analysis (equal); Funding acquisition (equal); Project administration (equal); Supervision (equal); Writing – review & editing (equal).

DATA AVAILABILITY

The data that support the findings of this study are available from the corresponding author upon reasonable request.

REFERENCES

[1]J. Aguilar-Cabello, P. Gutierrez-Castillo, L. Parras, C. del Pino, and E. Sanmiguel-Rojas, "On the onset of negative lift in a symmetric airfoil at very small angles of attack," Phys. Fluids **32**(5), 055107 (2020).
[2]J. Aguilar-Cabello, L. Parras, and C. del Pino, "DPIVSoft-Opencl: A multicore CPU–GPU accelerated open-source code for 2D particle image velocimetry," SoftwareX **20**, 101256 (2022).
[3]J. D. Anderson, *Fundamentals of Aerodynamics*, 6th ed. (McGraw-Hill Education, 2016).
[4]A. Antkowiak and P. Brancher, "Transient energy growth for the Lamb–Oseen vortex," Phys. Fluids **16**(1), L1–L4 (2004).
[5]M. Anyoji, M. Okamoto, H. Hidaka, K. Kondo, A. Oyama, H. Nagai, and K. Fujii, "Control surface effectiveness of low Reynolds number flight vehicles," JFST **9**(5), JFST0072–JFST0072 (2014).
[6]G. Batchelor, "Axial flow in trailing line vortices," J. Fluid Mech. **20**(4), 645–658 (1964).
[7]F. J. Blanco-Rodríguez, L. Parras, and C. del Pino, "Frequency response of Lamb-Oseen vortex," Fluid Dyn. Res. **48**, 061417 (2016).
[8]F. J. Blanco-Rodríguez, J. O. Rodríguez-García, L. Parras, and C. del Pino, "Optimal response of Batchelor vortex," Phys. Fluids **29**(6), 064108 (2017).
[9]T. Bölle, V. Brion, M. Couliou, and P. Molton, "Experiment on jet-vortex interaction for variable mutual spacing," Phys. Fluids **35**(1), 015117 (2023).

[10]T. Bölle, V. Brion, J.-C. Robinet, D. Sipp, and L. Jacquin, "On the linear receptivity of trailing vortices," J. Fluid Mech. **908**, A8 (2021).
[11]K. Chang, H. Chen, T. Tzong, and T. Cebeci, "Prediction of aeroelastic effects of aircraft configurations including high lift systems," ICAS Paper (2000).
[12]T.-Y. Chiu, C.-C. Tseng, C.-C. Chang, and Y.-J. Chou, "Vorticity forces of coherent structures on the NACA0012 aerofoil," J. Fluid Mech. **974**, A52 (2023).
[13]J. N. N. Counsil and K. Goni Boulama, "Low-Reynolds-number aerodynamic performances of the NACA 0012 and Selig–Donovan 7003 airfoils," J. Aircraft **50**(1), 204–216 (2013).
[14]Y. Dai, Y. Xia, G. Huang, C. Yang, and Y. Li, "Performance improvement of a wing with a controlled spanwise bending wingtip," Ocean Eng. **287**, 115795 (2023).
[15]C. del Pino, J. López-Alonso, L. Parras, and R. Fernandez-Feria, "Dynamics of the wing-tip vortex in the near field of a NACA 0012 aerofoil," Aeronaut. J. **115**(1166), 229–239 (2011a).
[16]C. del Pino, L. Parras, M. Felli, and R. Fernandez-Feria, "Structure of trailing vortices: Comparison between particle image velocimetry measurements and theoretical models," Phys. Fluids **23**(1), 013602 (2011b).
[17]M. Dghim, M. Ferchichi, and H. Fellouah, "Mid-wake wing tip vortex dynamics with active flow control," Exp. Therm. Fluid Sci. **98**, 38–55 (2018).
[18]A. M. Edstrand, T. B. Davis, P. J. Schmid, K. Taira, and L. N. Cattafesta, "On the mechanism of trailing vortex wandering," J. Fluid Mech. **801**, R1 (2016).
[19]Y.-H. Fang, C.-H. Tang, Y.-J. Lin, S.-I. Yeh, and J.-T. Yang, "The lift effects of chordwise wing deformation and body angle on low-speed flying butterflies," Biomimetics **8**(3), 287 (2023).
[20]J. A. Farnsworth, S. Corbett, J. Seidel, and T. E. McLaughlin, "Aeroelastic response of a finite span NACA 0018 wing. Part 1: Experimental measurements," In *53rd AIAA Aerospace Sciences Meeting* (AIAA, 2015), p. 0249.
[21]J. H. García-Ortiz, A. Domínguez-Vázquez, J. Serrano-Aguilera, L. Parras, and C. del Pino, "A complementary numerical and experimental study of the influence of Reynolds number on theoretical models for wingtip vortices," Comput. Fluids **180**, 176–189 (2019).
[22]J. H. García-Ortiz, F. J. Blanco-Rodríguez, L. Parras, and C. del Pino, "Experimental observations of the effects of spanwise blowing on the wingtip vortex evolution at low Reynolds numbers," Eur. J. Mech. B Fluids **80**, 133–145 (2020).
[23]P. Gutierrez-Castillo, M. Garrido-Martin, T. Bölle, J. H. García-Ortiz, J. Aguilar-Cabello, and C. del Pino, "Higher order dynamic mode decomposition of an experimental trailing vortex," Phys. Fluids **34**(10), 107116 (2022).
[24]N. T. Hoang, "Computational investigation of variation in wing aerodynamic load under effect of aeroelastic deformations," J. Mech. Sci. Technol. **32**, 4665–4673 (2018).
[25]S. F. Hoerner, *Fluid-Dynamic Drag: Practical Information on Aerodynamic Drag and Hydrodynamic Resistance*, 2nd ed. (Hoerner Fluid Dynamics, Midland Park, NJ, 1958).
[26]I. Kursakov, E. Kazhan, and R. Gebbink, "Computational study of wing deformation and sting interference effects with the CAE-AVM test case," Chin. J. Aeronaut. **31**(10), 1954–1961 (2018).
[27]T. Lee and J. Pereira, "Modification of static-wing tip vortex via a slender half-delta wing," J. Fluids Struct. **43**, 1–14 (2013).
[28]Y.-C. Liu and F.-B. Hsiao, "Experimental investigation on critical Reynolds numbers aerodynamic properties of low aspect ratios wings," Procedia Eng. **79**, 76–85 (2014).
[29]L. Mendes, A. Bernardino, and R. M. Ferreira, "PIV-image-generator: An image generating software package for planar PIV and optical flow benchmarking," SoftwareX **12**, 100537 (2020).
[30]P. Meunier and T. Leweke, "Analysis and treatment of errors due to high velocity gradients in particle image velocimetry," Exp. Fluids **35**, 408–421 (2003).
[31]D. W. Moore and P. G. Saffman, "Axial flow in laminar trailing vortices," Proc. R. Soc. Lond. A Math. Phys. Sci. **333**(1595), 491–508 (1973).
[32]T. Ohtake, Y. Nakae, and T. Motohashi, "Nonlinearity of the aerodynamic characteristics of NACA0012 aerofoil at low Reynolds numbers," J. Jpn. Soc. Aeronaut. Space Sci. **55**(644), 439–445 (2007).
[33]M. Okamoto, D. Sasaki, M. Kamikubo, and R. Fujii, "Disappearance of vortex lift in low-aspect-ratio wings at very-low Reynolds numbers∗," Trans. Jpn. Soc. Aero. Space Sci. **62**(6), 310–317 (2019).
[34]L. Prandtl, "Tragflügeltheorie. i. mitteilung," *Nachr. von der Gesellschaft der Wissenschaften zu Göttingen* (Mathematisch-Physikalische Klasse, 1918), pp. 451–477.
[35]C. Pranesh, M. Sivapragasam, M. Deshpande, and H. Narahari, "Negative lift characteristics of NACA 0012 aerofoil at low Reynolds numbers," Sādhanā **44**(1), 21 (2019).
[36]N. Rashmi and M. Sivapragasam, "A boundary-vorticity perspective on lift enhancement at ultra-low Reynolds numbers," J. Aeros. Sci. Technol. **72**(2), 98–106 (2023).
[37]W. Roberts, "Calculation of laminar separation bubbles and their effect on airfoil performance," AIAA J. **18**(1), 25–31 (1980).
[38]T. A. Smith and Y. Ventikos, "Wing-tip vortex dynamics at moderate Reynolds numbers," Phys. Fluids **33**(3), 035111 (2021).
[39]J. Tank, L. Smith, and G. R. Spedding, "On the possibility (or lack thereof) of agreement between experiment and computation of flows over wings at moderate Reynolds number," Interface Focus **7**(1), 20160076 (2017).
[40]C. E. Toppings and S. Yarusevych, "Structure and dynamics of a laminar separation bubble near a wingtip," J. Fluid Mech. **929**, A39 (2021).
[41]L. W. Traub, "Aerodynamic impact of aspect ratio at low Reynolds number," J. Aircraft **50**(2), 626–634 (2013).
[42]L. W. Traub, "Examination and prediction of the lift components of low aspect ratio rectangular flat plate wings," Aerospace **10**(7), 597 (2023).
[43]L. W. Traub and C. Coffman, "Efficient low-Reynolds-number airfoils," J. Aircraft **56**(5), 1987–2003 (2019).
[44]T. Tsuchiya, D. Numata, T. Suwa, and K. Asai, "Influence of turbulence intensity on aerodynamic characteristics of an NACA 0012 at low Reynolds numbers," in *51st AIAA Aerospace Sciences Meeting Including the New Horizons Forum and Aerospace Exposition* (AIAA, 2013), p. 65.
[45]S. Wang, Y. Zhou, M. M. Alam, and H. Yang, "Turbulent intensity and Reynolds number effects on an airfoil at low Reynolds numbers," Phys. Fluids **26**(11), 115107 (2014).
[46]J. Winslow, H. Otsuka, B. Govindarajan, and I. Chopra, "Basic understanding of airfoil characteristics at low Reynolds numbers (10 4–10 5)," J. Aircraft **55**(3), 1050–1061 (2018).
[47]T. Xia, H. Dong, L. Yang, S. Liu, and Z. Jin, "Investigation on flow structure and aerodynamic characteristics over an airfoil at low Reynolds number – A review," AIP Adv. **11**(5), 050701 (2021).
[48]M. Xu, H. Cheng, B. Ji, and X. Peng, "Prediction method of tip vortex circulation based on hydrofoil load," Ocean Eng. **288**, 116176 (2023).
[49]T. Yasuda, K. Fukui, K. Matsuo, H. Minagawa, and R. Kurimoto, "Effect of the Reynolds number on the performance of a NACA0012 wing with leading edge protuberance at low Reynolds numbers," Flow. Turbul. Combust. **102**, 435 (2019).
[50]K. Yonemoto, K. Takato, H. Ochi, and S. Fujie, "Kutta condition violation in two-dimensional NACA0012 airfoil at low Reynolds number," in *26th AIAA Applied Aerodynamics Conference* (2008).
[51]H. Yu, U. Ciri, A. S. Malik, and S. Leonardi, "Decoupled effects of localized camber and spanwise bending for flexible thin wing," AIAA J. **58**(5), 2293–2306 (2020).
[52]M. Zaccara, P. Bragana, C. Cuvier, G. Paolillo, T. Astarita, G. Cardone, J.-M. Foucaut, and C. S. Greco, "Far field behaviour of wingtip vortices under synthetic jet-based control," Aeros. Sci. Technol. **143**, 108755 (2023).
[53]M. Zhong, S. Zheng, W. Ganglin, H. Jun, and R. Gebbink, "Correlation analysis of combined and separated effects of wing deformation and support system in the CAE-AVM study," Chin. J. Aeronaut. **31**(3), 429–438 (2018).